

ARTICLES

Metallization cross-linking and electronic state engineering of zeolitic imidazole framework: boosting the electroanalytical response of physiological biomolecules

Wang Sun^{1†}, Na Wang^{3†}, Junyan Liu¹, Guorong Sun¹, Joshua Phipps², Thamraa AlShahrani⁴, Shengqian Ma^{2*} & Yang Wang^{1*}¹School of Chemistry and Chemical Engineering, Yangzhou University, Yangzhou 225002, China²Department of Chemistry, University of North Texas, Denton, TX 76201, USA³Key Laboratory of Systems Biomedicine (Ministry of Education), Shanghai Center for Systems Biomedicine, Shanghai Jiao Tong University, Shanghai 200240, China⁴Department of Physics, College of Science, Princess Nourah bint Abdulrahman University, Riyadh 11564, Saudi Arabia

†Equally contributed to this work.

*Corresponding authors (email: shengqian.ma@unt.edu; wangyzu@126.com)

Received 29 June 2025; Accepted 31 July 2025; Published online 16 October 2025

Abstract Utilizing the Kirkendall effect to acquire hollow zeolitic imidazole framework (HZIF) allows for the predictable combination of superior guest molecules, which has favorable potential in the field of biomolecular detection. Herein, the ~42 nm hollow nanocages, HZIF(Au), were constructed through the different diffusion rates of Zn²⁺ and Au³⁺. By leveraging the Kirkendall effect at different Au³⁺ levels and over time (0, 5, 30, and 60 min) a composite with iron porphyrin (TCPP(Fe)) (the HZIF(Au_{4.5})@TCPP(Fe)) was effectively assembled. The selection of various metals within HZIF(Au_{4.5})@TCPP(Fe)-M (M = Fe, Co, Ni, and Cu) hybrid nanocomposites was then successfully formed via metallization cross-linking engineering. This metallization and the electron-donating properties of TCPP resulted in an electron-rich state for Au while the cross-linking of the carboxyl groups of TCPP with metal ions also significantly improved the electrocatalytic performance. Together, this allowed HZIF(Au_{4.5})@TCPP(Fe)-Fe to act as an effective electrochemical sensor with dopamine (DA) as the target molecule. In the optimal electrolyte environment, the linear range of 0.006–1500 μmol L⁻¹ and detection limit of 0.002 μmol L⁻¹ (signal-to-noise ratio, S/N = 3) could be realized for the DA response. This study carried out the fine regulation of ZIF nanocrystals through rational design; the unique construction and assembly strategy offered here will open up new routes for the evaluation of disease markers to effectively identify and monitor disease.

Keywords hollow ZIF, Kirkendall effect, iron porphyrin, electrochemical detection, dopamine

1 Introduction

Nanocrystals with controllably constructed high crystallinity, abundant active centers, and tailored local microenvironments present incredible potential in the fields of energy storage, sensing, and catalysis [1,2]. As classical porous coordinated nanocrystals, metal-organic frameworks (MOFs) are a class of classical porous coordinated nanocrystals and are assembled from organic linkers and metal nodes/clusters and represent ideal platforms for these applications [3–7]. The exploration of customization in solid MOFs has been well studied with such adjustments as doping, modification, derivatization, functionalization, and formation of heterojunctions [8–12]. With the rapid evolution of organic-inorganic hybrid nanomaterials, hollow MOFs, as the optimized product of solid MOFs, have become increasingly notable for their performance. Their unique hollow cavities endow the material with greater porosity, allowing for a richer density of active sites, faster substance transport, and better compatibility [13]. Presently, most of the strategies for the construction of hollow MOFs include weak-acid/base etching, soft/hard template methods, and precursor conversion approaches [14,15]. It is worth noting that these classic paths carry certain limitations including: (1) the sensitivity of MOFs to etching agents, which can easily cause the collapse of the overall frame structure; (2) the use of etching agents can lead to potentially harmful effects on the environment and human health; (3) the lack

of controllability when growing MOFs on a template; (4) the difficulty in controlling the shape and composition of MOFs. These factors necessitate the discovery of alternative and novel routes for the construction of hollow MOFs to improve their efficacy for a diverse array of applications.

Recent studies have revealed that the Kirkendall effect may be leveraged as a facile and effective strategy for acquiring hollow cavities within mesoporous nanoparticles [16]. Specifically, this effect occurs when there is a difference in diffusion rates between two components of a diffusion couple, leading to the formation of defects at the interface, thereby generating a distinct hollow structure [17]. The Kirkendall effect can be categorized as a “self-template” approach, where the template can be automatically depleted during the hollowing procedure, allowing for several advantages, including access to high-quality nanocrystals of uniform size and shape, relatively high crystallinity, and straightforward operation. At present, the Kirkendall effect has mainly been applied in metal compounds/metal nanoparticles, *e.g.*, metal phosphides, metal sulfides, metal nitrides, and metal oxides [18,19]. However, the study of this effect with respect to MOFs is relatively new. This newfound customization afforded to MOFs creates a valuable ability to regulate the presence and size of hollow cavities within MOFs, imparting new characteristics to the material while maintaining the exceptional advantages of the framework offers.

Citation: Sun W, Wang N, Liu J, Sun G, Phipps J, AlShahrani T, Ma S, Wang Y. Metallization cross-linking and electronic state engineering of zeolitic imidazole framework: boosting the electroanalytical response of physiological biomolecules. *Sci China Chem*, 2026, 69: 1784–1793. <https://doi.org/10.1007/s11426-025-2932-5>

The introduction of guest materials within hollow MOFs can be utilized to further improve the overall performance in a range of applications. For example, Metalloporphyrins (*e.g.*, $C_{48}H_{28}ClFeN_4O_8$, TCPP(Fe)) can be introduced within these pores as ideal guest molecules with their classical cyclic conjugated structure, excellent thermal/electronic stability, modifiability, good catalytic activities, and outstanding redox properties [20–23]. This addition and electron-donating characteristics of TCPP may endow the guest molecule with a unique electronic state. Additionally, the modification of TCPP(Fe) may lead to greater accessibility of the cross-linked metal on the surface, which is conducive to improving its interaction with target molecules, further improving the desired catalytic performance. This integrated strategy combining hollow MOFs, the Kirkendall effect, and the inclusion of modified guest molecules holds fascinating potential in the field of electroanalytical detection.

Herein, based on the excellent cost-effectiveness, operability and good thermal/chemical stability of ZIF-8, it was selected as a candidate in this study. The HZIF(Au_{4.5})@TCPP(Fe)-M (M = Fe, Co, Ni and Cu) were successfully fabricated utilizing the Kirkendall effect and metallization cross-linking engineering. The hollow structures could be formed quickly (~1 h) without the need for chemical acid/base etchants or soft/hard templates. The screen-printed electrodes (SPE) were then modified via as-constructed hollow nanocrystals and connected to a portable electrochemical workstation. Next, dopamine ($C_8H_{11}NO_2$, DA), a classic physiological biomolecule, was selected as a model for study. This endogenous nitrogen-containing neurotransmitter plays a key regulatory role in the central nervous system [24,25] and is an important biomolecule in organisms involved in normal physiological functions and vital activities, representing an excellent case study to examine the advantages of electrochemical sensing (*e.g.*, rapid response, ease of operation) [26–29]. To perform this evaluation, a novel electrochemical sensor for quick and efficient detection of DA was fabricated and the electrochemical performance in the detection of DA, the electrode comparison, scan rate, pH and linear range were each explored. This revealed an optimal enrichment potential/time that improved the current response toward DA in both simulated conditions and actual samples. Together, this effective combination of porous coordination polymers, the Kirkendall effect, and inclusion of metalloporphyrins provides a novel perspective for the advancement of electrochemical sensors.

2 Experimental

2.1 Chemicals

The analytical reagents in this study are abbreviated as AR. Zinc nitrate hexahydrate ($Zn(NO_3)_2 \cdot 6H_2O$, AR), cobalt chloride hexahydrate ($CoCl_2 \cdot 6H_2O$, AR), nickel chloride hexahydrate ($NiCl_2 \cdot 6H_2O$, AR), copper chloride dihydrate ($CuCl_2 \cdot 2H_2O$, AR) and $H AuCl_4 \cdot 4H_2O$ ($\geq 47.8\%$, AR) were purchased from Sinopharm Chemical Reagent (Shanghai, China). Disodium hydrogen phosphate dodecahydrate ($Na_2HPO_4 \cdot 12H_2O$, AR), iron trichloride hexahydrate ($FeCl_3 \cdot 6H_2O$, 99%), dopamine ($C_8H_{11}NO_2$, 98%), sodium phosphate dihydrate ($NaH_2PO_4 \cdot 2H_2O$, AR), Fe(III) meso-tetra (4-carboxyphenyl) porphyrin chloride (TCPP(Fe), 95%) and 2-methylimidazole ($C_4H_6N_2$, 98%) were obtained via Aladdin Chemical Reagent (Shanghai, China). Methanol (CH_3OH , AR) and β -mercaptoethylamine (C_2H_7NS , 95%) were purchased through Macklin Reagent (Shanghai, China). Of note, all reagents were used directly without any special treatment.

2.2 Synthesis of ZIF-8

The ZIF-8 was prepared via the previously reported method of the research group [30]. Specifically, 0.84 mmol $Zn(NO_3)_2 \cdot 6H_2O$ was dispersed in 6.25 mL methanol, called solution (I). 10.7 mmol 2-methylimidazole was fully dissolved in 12.5 mL methanol, called solution (II). Then, the obtained I and II were mixed uniformly and stirred continuously for 12 h. Eventually, the white suspension was washed four times by centrifugation (400 mL methanol, 9500 r/min, 3 min) and vacuum dried at 60 °C for 12 h.

2.3 Synthesis of HZIF(Au_{4.5}) and HZIF(Au_{1.5})

The HZIF(Au_{4.5}) was acquired through the Kirkendall effect. At first, the synthesized ZIF-8 (50 mg) was thoroughly dispersed in 45 mL of methanol through sonication. Then, 4.5 mL of $H AuCl_4 \cdot 4H_2O$ (0.02 g mL^{-1}) was slowly added to the above dispersed solution and stirred vigorously for 1 h. Next, the obtained yellow solution was centrifugally washed several times (9500 r/min, 2 min) and dried at 60 °C for 12 h, and denoted as HZIF(Au_{4.5}). Similarly, the preparation of HZIF(Au_{1.5}) also followed the above procedure, except that the $H AuCl_4 \cdot 4H_2O$ introduced into the system was 1.5 mL. Notably, the samples collected at 5 and 30 min were denoted as HZIF(Au_{4.5})-5 min, HZIF(Au_{1.5})-5 min, HZIF(Au_{4.5})-30 min, and HZIF(Au_{1.5})-30 min, respectively.

2.4 Preparation of HZIF(Au_{4.5})@TCPP(Fe) and HZIF(Au_{4.5})@TCPP(Fe)-M (M = Fe, Co, Ni, and Cu)

Relevant samples were constructed with reference to the literature and accompanying modifications [31]. Firstly, ~0.1 g HZIF(Au_{4.5}) was added to 100 mL of methanol and sonicated for 10 min. Subsequently, 0.02 g of β -mercaptoethylamine was introduced into the above solution and stirred continuously for 8 h. When stirring was finished, the solution was washed three times with methanol and dried at 60 °C for 12 h. Next, the obtained sample and 5 mg of TCPP(Fe) were dispersed into 20 mL of methanol with continuous stirring for 24 h. Finally, the collected samples were washed several times with methanol and dried overnight (60 °C), and marked as HZIF(Au_{4.5})@TCPP(Fe). As for the preparation of HZIF(Au_{4.5})@TCPP(Fe)-M (M = Fe, Co, Ni, and Cu): firstly, 0.05 g HZIF(Au_{4.5})@TCPP(Fe) was introduced into 50 mL of methanol solution and sonicated for 15 min. In the second step, an equimolar amount (0.011 mmol) of Fe^{3+} or Co^{2+} or Ni^{2+} or Cu^{2+} was added to the above solution and stirred vigorously for 8 h. Finally, the collected samples (*i.e.*, HZIF(Au_{4.5})@TCPP(Fe)-M (M = Fe, Co, Ni, and Cu)) were washed several times via centrifugation and dried at 60 °C for 12 h. Similarly, the introduction of different levels of Fe^{3+} into this system also followed the above-mentioned steps. When the Fe^{3+} content was 0.022 mmol (~6 mg) and 0.033 mmol (~9 mg), the acquired samples were named HZIF(Au_{4.5})@TCPP(Fe)-Fe₆ and HZIF(Au_{4.5})@TCPP(Fe)-Fe₉, respectively.

The detailed description of the apparatus, electrode modification process, and equations is available in the Supporting Information online. For the series of samples constructed in this research, the full details of all materials used and synthetic protocols can be found in Table S1 (Supporting Information online).

3 Results and discussion

3.1 Morphological analysis and structural characterization of samples

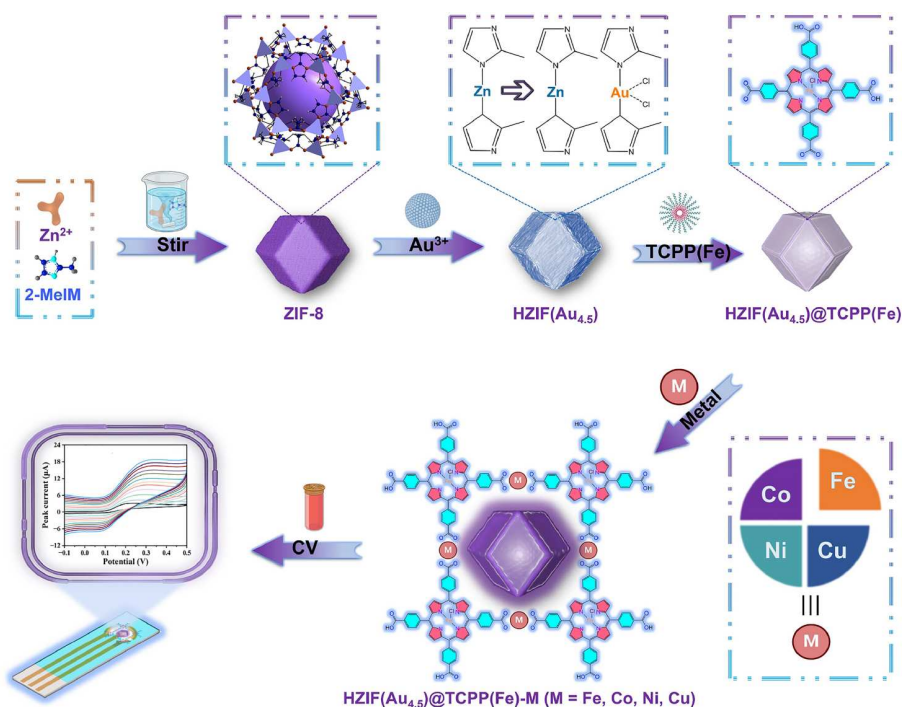
The process HZIF(Au_{4.5})@TCPP(Fe)-M (M = Fe, Co, Ni, Cu)

synthesis is illustrated in Scheme 1. Following successful synthesis of the parent ZIF-8 MOF, cation exchange of the Zn^{2+} and Au^{3+} was performed (Figure S1, Supporting Information online). This resulted in the predicted evolution of the MOF structure leveraging the Kirkendall effect. This process and the mechanism of structural evolution are illustrated in Figure 1a. Meanwhile, the non-equilibrium mutual diffusion phenomena were also observed during this exchange reaction. In Figure 1a, as the rate of outward diffusion of Zn^{2+} through the shell layer is superior to the rate of inward diffusion of Au^{3+} , the Kirkendall cavities are formed. As the diffusion process continues, the hollow frame structure is eventually produced [32]. This kinetic process of the transition of solid nano-MOFs to hollow structures was explored in this study using transmission electron microscopy (TEM). To evaluate the effect of cation concentration on the solid ZIF-8, the MOF was subjected to increasing concentrations of chloroauric acid aqueous solution (1.5 or 4.5 mL, $C_{\text{Au}} = 0.02 \text{ g mL}^{-1}$), followed by an observation of the microscopic characteristics of the samples at 0, 5, 30, and 60 min, respectively. At 0 min, the initial state of ZIF-8, *i.e.*, when no aqueous chloroauric acid solution was introduced, showed the solid rhombic dodecahedral structures (Figure 1b, f). Then at 5 min, the outer surfaces of HZIF($\text{Au}_{1.5}$) and HZIF($\text{Au}_{4.5}$) appeared to become smooth, and the solid nanostructures were maintained (Figure 1c, g). Here, the Au ions were mainly concentrated on the surface of the MOFs, however, as time increased to 30 min, the two nanomaterials showed the characteristics of being partially hollow, with the increased degree of hollowness for HZIF($\text{Au}_{4.5}$) (Figure 1h) compared to that of HZIF($\text{Au}_{1.5}$) (Figure 1d). Finally, at 60 min, the hollow cavities of HZIF($\text{Au}_{1.5}$) became more pronounced, but were irregular, asymmetric, and inhomogeneous (Figure 1e). In contrast, the HZIF($\text{Au}_{4.5}$) were relatively homogeneous with regular hollow cavities with a consistent size of approximately 42 nm (Figure 1i). Additionally, the elemental mapping results in Figure 1j, k also revealed the existence of the C, N, O, Zn, and Au elements in both HZIF($\text{Au}_{1.5}$) and HZIF($\text{Au}_{4.5}$) nanomaterials.

Following this experiment, a series of MOF nanocrystals (ZIF-8, HZIF($\text{Au}_{4.5}$), HZIF($\text{Au}_{4.5}$)@TCPP(Fe) and HZIF($\text{Au}_{4.5}$)@TCPP(Fe)-

Fe) were analyzed to evaluate the effect that guest molecules (TCPP) and the variation of metals species (Fe, Co, Ni, and Cu) cross-linking with TCPP via metal-carboxylate coordination may have on the surrounding framework. A schematic illustrating these components coordinating to one another within the hollow MOF cavity can be found in Figure 2a–d. These were observed via scanning electron microscope (SEM) and TEM to identify any morphological features with several notable findings (Figure 2e–o). First, the synthesized ZIF-8 presented the solid and regular polyhedral morphology with dimensions of around 85 nm (Figure 2e, i). In HZIF($\text{Au}_{4.5}$), the ~42 nm cavities were acquired via the Kirkendall effect (Figure 2f, j). For both the HZIF($\text{Au}_{4.5}$)@TCPP(Fe) (Figure 2g, k) and HZIF($\text{Au}_{4.5}$)@TCPP(Fe)-Fe (Figure 2h, l) nanocomposites, there were clear hollow structures that could be easily observed (marked by the blue arrows). Meanwhile, the high-resolution TEM of Figure 2m revealed the presence of small-sized and uniformly distributed nanoparticles in HZIF($\text{Au}_{4.5}$)@TCPP(Fe)-Fe, which circled in red. In Figure 2n, the ordered lattice fringes could be observed and are accompanied by a Fourier transform illustrating a crystal plane spacing of about 0.24 nm, which can be categorized as the Au(111) facet [33,34]. Thus, from the above, it can be concluded that there are abundant Au nanoparticles in HZIF($\text{Au}_{4.5}$)@TCPP(Fe)-Fe with a particle size of approximately 2.5 nm. At the same time, the elemental mapping (Figure 2o) demonstrated the well-dispersed C, N, O, S, Zn, Au, and Fe elements in HZIF($\text{Au}_{4.5}$)@TCPP(Fe)-Fe. And the EDS spectrum was displayed in Figure S2. The microscopic images of various metal cross-linking and iron salt content cross-linking were also captured. Specifically, the SEM and TEM images of HZIF($\text{Au}_{4.5}$)@TCPP(Fe)-M (M = Co, Ni, and Cu), HZIF($\text{Au}_{4.5}$)@TCPP(Fe)-Fe₆, and HZIF($\text{Au}_{4.5}$)@TCPP(Fe)-Fe₉ can be observed in Figure S3. The hollow structures of a series of nanocomposites could be clearly observed via TEM.

As depicted in Figure 3a, a range of hybridized nanocrystals (HZIF($\text{Au}_{4.5}$), HZIF($\text{Au}_{4.5}$)@TCPP(Fe) and HZIF($\text{Au}_{4.5}$)@TCPP(Fe)-Fe) all retained the crystal structure of ZIF-8 [35,36]. Meanwhile, the X-ray diffraction (XRD) patterns of HZIF($\text{Au}_{4.5}$)@TCPP(Fe)-M (M = Co, Ni, Cu) and HZIF($\text{Au}_{4.5}$)@TCPP(Fe)-Fe_x ($x = 6$ or 9) showed characteristic peaks similar to ZIF-8 and can be found in Figure S4.



Scheme 1 (Color online) Schematic illustration for the preparation route of HZIF($\text{Au}_{4.5}$)@TCPP(Fe)-M (M = Fe, Co, Ni, Cu).

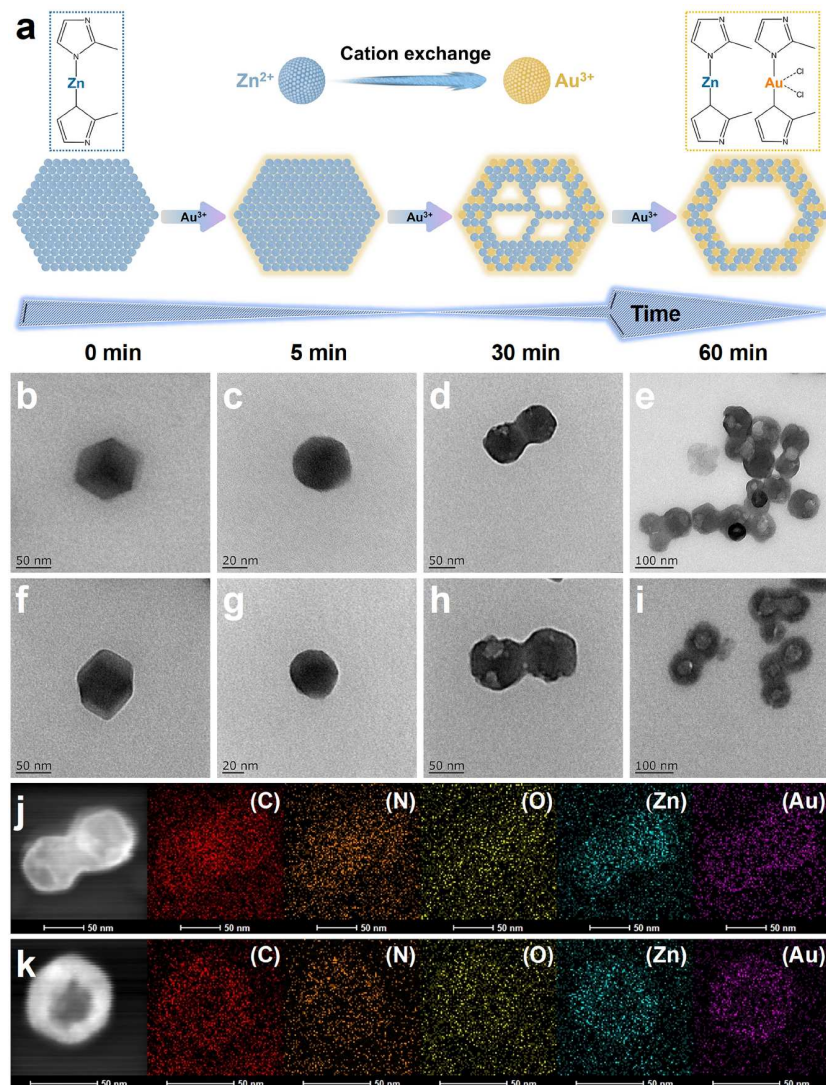


Figure 1 (Color online) (a) Schematic illustration of conversion from solid nano-polyhedron to hollow structures based on the Kirkendall effect. TEM images (0, 5, 30, and 60 min) of HZIF(Au_{1.5}) (b–e) and HZIF(Au_{4.5}) (f–i). Elemental mapping of HZIF(Au_{1.5}) (j) and HZIF(Au_{4.5}) (k).

In parallel to the synthesis of these materials, a series of nano-MOFs were also obtained using the Kirkendall effect at different times and were characterized via XRD (Figure S5). All the above-mentioned nanocomposites retained the initial characteristic crystal planes found in ZIF-8. Next, the Fourier transform-infrared spectroscopy (FTIR) of ZIF-8, HZIF(Au_{4.5}), HZIF(Au_{4.5})@TCPP(Fe), and HZIF(Au_{4.5})@TCPP(Fe)-Fe were conducted with the results illustrated in Figure 3b. Here we observed that an IR peak located at 421.2 cm⁻¹, which we classified as the classical stretching vibration between Zn–N. Next, the IR vibrations at 995.7, 1145.6, and 1174.9 cm⁻¹ were categorized as C–N bonds while the characteristic peaks at 1308.1 and 1221.8 cm⁻¹ each correspond to the stretching vibrations of C–H [37]. Finally, the IR peak near 3200 cm⁻¹ was tightly correlated with –NH₂. Simultaneously, the FTIR spectra (Figure S6) of HZIF(Au_{4.5})@TCPP(Fe)-M (M = Co, Ni, and Cu) and HZIF(Au_{4.5})@TCPP(Fe)-Fe_x (x = 6 or 9) all exhibited similar IR profiles, indicating a similar structural composition. Additionally, Figure 3c, d present the nitrogen adsorption and desorption curves and pore width distributions of ZIF-8, HZIF(Au_{4.5}), HZIF(Au_{4.5})@TCPP(Fe) and HZIF(Au_{4.5})@TCPP(Fe)-Fe, respectively. The detailed data for this procedure can be found in Table S2. Meanwhile, these results show that specific surface area decreased from: ZIF-8 > HZIF(Au_{4.5}) > HZIF(Au_{4.5})@TCPP(Fe) > HZIF(Au_{4.5})@TCPP(Fe)-Fe,

with the pore sizes of all materials in the range of <2 nm and 2–50 nm [38]. With regard to the thermal stability of samples, the HZIF(Au_{4.5})@TCPP(Fe)-Fe nanomaterial was also investigated using a thermogravimetric analysis (TGA) approach. The results showed a weight loss at 251 °C–584 °C which was ascribed to the decomposition of TCPP(Fe) and organic linkers [39,40] (Figure 3e). Compared to ZIF-8, the thermal stability of HZIF(Au_{4.5})@TCPP(Fe)-Fe was slightly decreased. There was also an increase in the Fe content in HZIF(Au_{4.5})@TCPP(Fe)-Fe compared to that of HZIF(Au_{4.5})@TCPP(Fe) in the ICP data (Figure 3f), which indicates the success of our metallization cross-linking strategy and the presence of our desired product. Next, the X-ray photoelectron spectroscopy (XPS) was applied to analyze the surface properties of the fabricated samples. As illustrated in Figure 3g, the HZIF(Au_{4.5})@TCPP(Fe)-Fe and HZIF(Au_{4.5}) both contained the C, N, O, S, Zn, Au, and Fe elements. As depicted in Figure 3h, the Au 4f orbitals of HZIF(Au_{4.5})@TCPP(Fe)-Fe were moved toward lower binding energy compared to HZIF(Au_{4.5}), which indicates that the Au in the HZIF(Au_{4.5})@TCPP(Fe)-Fe sample presents electron-rich states [41,42]. These Au 4f shifts were attributed to the fact that the iron-porphyrins possess electron-donor properties with delocalized π systems [43,44]. Together, these results suggest the existence of significant electronic state interactions in HZIF(Au_{4.5})@TCPP(Fe)-Fe.

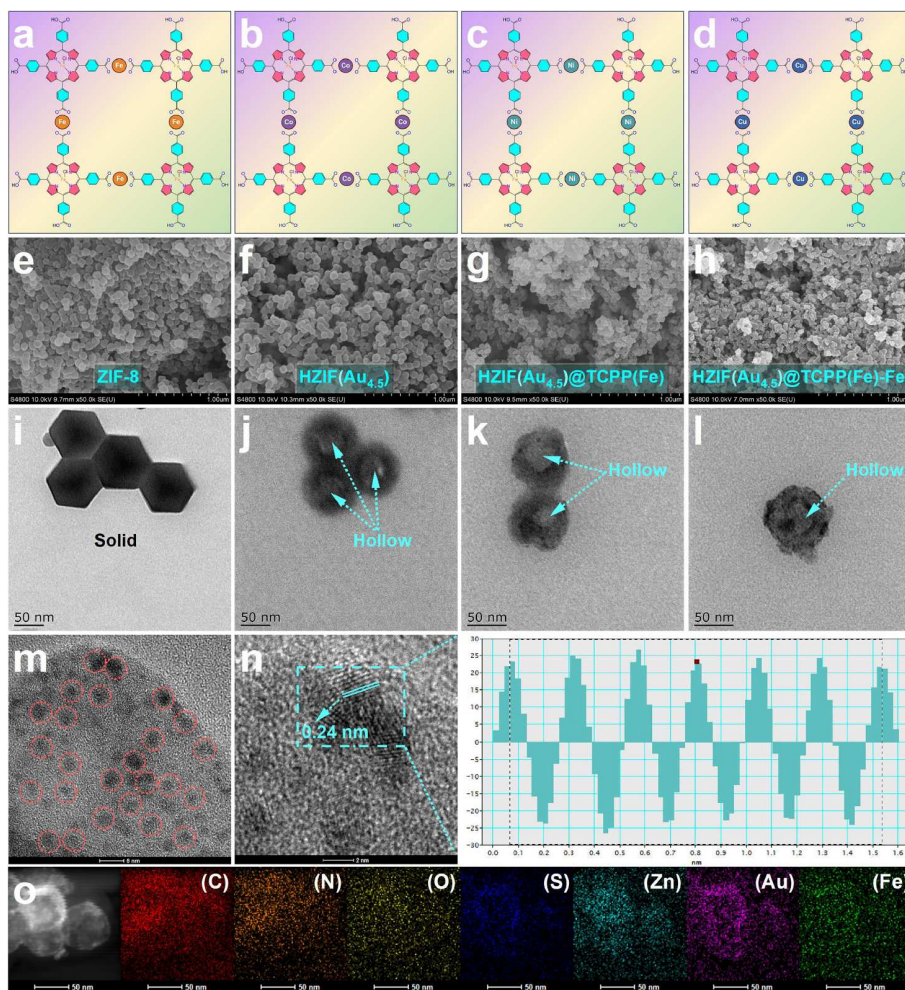


Figure 2 (Color online) (a–d) Description of metallization cross-linking engineering. SEM and TEM images of ZIF-8 (e, i), HZIF(Au_{4.5}) (f, j), HZIF(Au_{4.5})@TCPP(Fe) (g, k), and HZIF(Au_{4.5})@TCPP(Fe)-Fe (h, l). High resolution TEM (m), interplanar spacing (n), and elemental mapping (o) of HZIF(Au_{4.5})@TCPP(Fe)-Fe.

Additionally, we found that the Fe was mainly available in HZIF(Au_{4.5})@TCPP(Fe)-Fe in the form of Fe²⁺ and Fe³⁺ [45] (Figure S3) and is accompanied by a satellite peak, which is mainly caused by the multiple frequencies of the X-ray sources. Finally, the XPS peak at 530.18 eV was attributed to Fe–O (Figure S7), which originates from the coordination of the carboxylate group of TCPP and the additional introduced iron salts, and further supports the creation of our desired product [31]. The elemental contents and Zn 2p curves in HZIF(Au_{4.5})@TCPP(Fe)-Fe can be seen in Table S3 and Figure S8, respectively. When combined, the results from the above characterization methods indicate the success of our metallization and cross-linking strategy.

3.2 Electroanalytical evaluation of DA at a series of modified electrodes

The electrochemical behaviors in this study were performed using the mini portable electrochemical workstation and the corresponding electrode adapters, which can be observed in Figure S9. Prior to sample analysis, differential pulse voltammetry (DPV) was utilized to determine the electrode material with the optimal DA response. During this test, we found that the current signal of HZIF(Au_{4.5})/SPE was significantly better than that of HZIF(Au_{1.5})/SPE (Figure S11). When we tested the electrochemical performance of HZIF(Au_{4.5})@TCPP(Fe)-M (M = Cu, Ni, Co, and Fe) and different levels of Fe salts modification (HZIF(Au_{4.5})@TCPP(Fe)-Fe, HZIF(Au_{4.5})

@TCPP(Fe)-Fe_x (x = 6 or 9), the HZIF(Au_{4.5})@TCPP(Fe)-Fe presented the best DA electrocatalytic behavior and was selected as the focus of this study (Figures S11 and S12).

Following the selection of electrode material, we investigated a series of reaction kinetics around DA. In Figure 4a, b, the response sequence of different modified electrodes to DA was as follows: HZIF(Au_{4.5})@TCPP(Fe)-Fe/SPE (16.7 μA) > HZIF(Au_{4.5})@TCPP(Fe)/SPE (12.2 μA) > HZIF(Au_{4.5})/SPE (6.0 μA) > ZIF-8/SPE (2.4 μA) > SPE (1.23 μA). When we measured the cyclic voltammetry (CV) curves of the above four modified electrodes, we found that there was no current response when no DA was present in the electrolyte solution (Figure S13). This indicates that the HZIF(Au_{4.5})@TCPP(Fe)-Fe/SPE can substantially enhance the signal response of DA.

We then evaluated the influence that different scan rates had on the electroanalytical sensor (Figure 4c, d). Here we found that as the scan rates (v) increased from 25 to 550 mV s⁻¹, the profiles of DA response became more pronounced, and with a significant increase in the peak currents of both the cathodic (I_{pc}) and anodic (I_{pa}) responses. And the response of the HZIF(Au_{4.5})@TCPP(Fe)-Fe electrochemical sensor to the DA peak current has a significant linear relationship with the v^{1/2} [46]. Based on this, the electroanalytical assessment of DA is a diffusion control process. The fitted equations (Eqs. (S1) and (S2)) can be seen in the Supporting Information. When evaluating these plots, a clear linear relationship between anode or cathode peak potential (E_{pa} or E_{pc}) and lnv can be observed (Figure 4e).

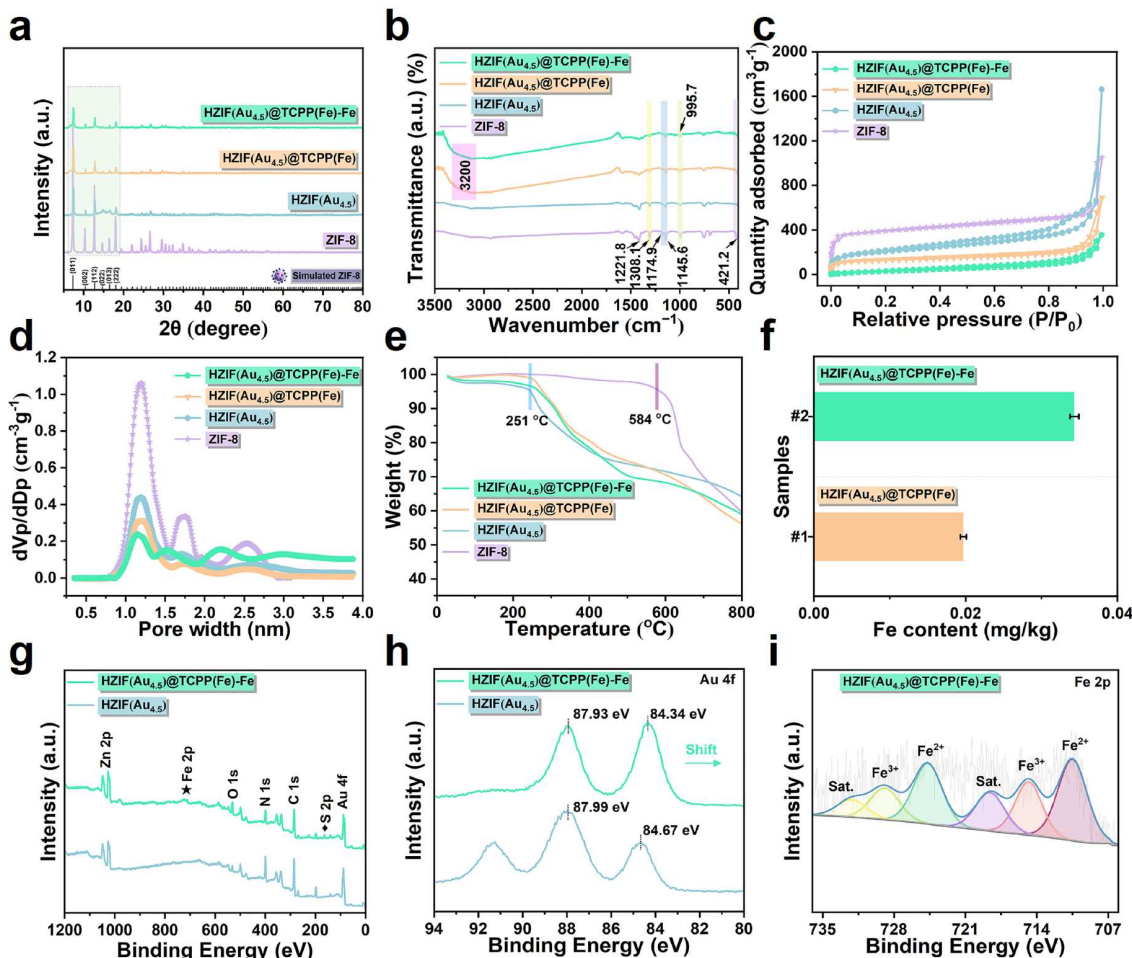


Figure 3 (Color online) XRD profiles (a), FTIR spectra (b), N_2 adsorption-desorption curves (c), pore width distributions (d), TG patterns (e) of ZIF-8, HZIF(Au_{4.5}), HZIF(Au_{4.5})@TCPP(Fe), and HZIF(Au_{4.5})@TCPP(Fe)-Fe. (f) ICP analysis of HZIF(Au_{4.5})@TCPP(Fe) and HZIF(Au_{4.5})@TCPP(Fe)-Fe. XPS broad spectrum (g) and Au 4f (h) of HZIF(Au_{4.5}) and HZIF(Au_{4.5})@TCPP(Fe)-Fe. (i) Fe 2p of HZIF(Au_{4.5})@TCPP(Fe)-Fe with the satellite (Sat.) region denoted.

Next, we investigated the influence of varying pH on the electroanalytical system. From this, we found that the optimal pH with the strongest DA response from HZIF(Au_{4.5})@TCPP(Fe)-Fe/SPE occurred at pH 7.4 (Figure 4f). We also found a functional relationship between the potential (E_{pa}) and pH (Figure 4g), which can be described by the equation (Eq. (S3)). The slope of this equation (50.1 mV pH^{-1}) was very near to the theoretical value (59.0 mV pH^{-1}) calculated from the Nernst equation (Eq. (S4)). We also calculated the electron transfer number using Eq. (S5) and found that $n = 2.37$ ($n \approx 2$) during the detection process.

Chronocoulometry is primarily performed to determine the adsorption situation at the electrode interface and allows for the identification of the effective region of the electrode (ERE), which is crucial for an in-depth understanding of the entire electrocatalytic process. As an aid to understand this electrocatalytic process, we created Figure 5 and Figure S14 to illustrate the reaction pathway of DA on the sensor. The ERE values we obtained are tightly related to electrochemical characteristics, such as sensitivity, reaction rate, and response interval. To evaluate ERE values, we utilized Anzon's equation (Eq. (S6)), and found there was an increase in this value as we progressed from SPE, ZIF-8/SPE, HZIF(Au_{4.5})/SPE, HZIF(Au_{4.5})@TCPP(Fe)/SPE, and HZIF(Au_{4.5})@TCPP(Fe)-Fe/SPE with corresponding values of 0.006, 0.01, 0.025, 0.041, and 0.062 cm^2 , respectively. For further testing, the charge parameters (Q) of SPE, ZIF-8/SPE, HZIF(Au_{4.5})/SPE, HZIF(Au_{4.5})@TCPP(Fe)/SPE, and HZIF(Au_{4.5})@TCPP(Fe)-Fe/SPE were evaluated and found that all

displayed the obvious linear positive correlation with the square root of time ($t^{1/2}$) (Figure 4h, i). These results indicate that the electrode surface of HZIF(Au_{4.5})@TCPP(Fe)-Fe/SPE has the highest ERE value, allowing more active sites for the electrocatalytic reaction of DA. When we calculated the diffusion coefficient of DA, according to the Cottrell equation (Eq. (S7)), we found there was a rate of $6.513 \times 10^{-6} \text{ cm}^2 \text{ s}^{-1}$. And the electron transfer rate constant for dopamine oxidation as 0.566 s^{-1} via the Laviron equation (Eq. (S8)). We then plotted the relationship between increasing sample concentrations (0, 100, 200, 300, 400 $\mu\text{mol L}^{-1}$ of DA) and time (t) (Figure 4j) as well as the peak current on the HZIF(Au_{4.5})@TCPP(Fe)-Fe/SPE under these same conditions (Figure 4k). These results showed a significant positive correlation with $t^{-1/2}$. Additionally, we found that the slope (derived from Figure 4k) had a markedly linear relationship with DA concentration (Figure 4l).

Next, we explored the sensitivity of the fabricated HZIF(Au_{4.5})@TCPP(Fe)-Fe electroanalytical sensing platform via accumulating potential and time. These two factors are tightly correlated with the linear interval and detection limits of the analyte. As depicted in Figure S15a, the peak current exhibited a parabolic peak starting at -0.1 V and ending at 0.3 V with a maximum at 0.1 V , indicating a favorable accumulation potential for the electrochemical analysis of DA within this range. As exposure of DA to the sensor progressed over time, we observed that this current increased until reaching a limit after 150 s at which there appeared to be no further increase,

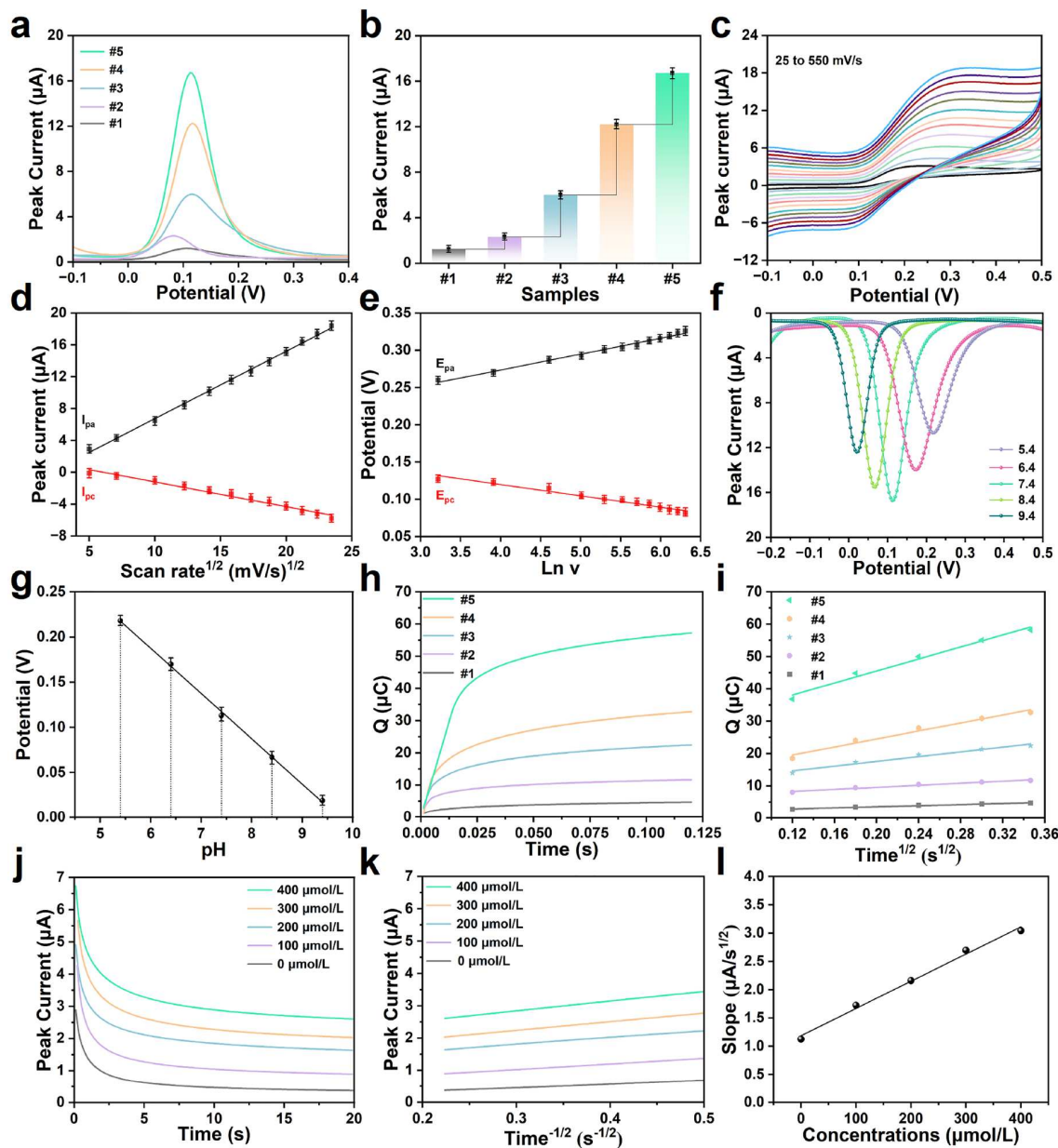


Figure 4 (Color online) (a) DPV values of synthesized materials (SPE (#1), ZIF-8/SPE (#2), HZIF(Au_{4.5})/SPE (#3), HZIF(Au_{4.5})/TCPP(Fe)/SPE (#4), and HZIF(Au_{4.5})/TCPP(Fe)-Fe/SPE (#5)) in 0.1 mol L⁻¹ PBS ($C_{\text{DA}} = 100 \mu\text{mol L}^{-1}$). (b) The specific peak current data. (c) CV curves of HZIF(Au_{4.5})/TCPP(Fe)-Fe/SPE at various scan rates (25–550 mV s⁻¹). (d) The correlation between current response and scan rates. (e) Linear behaviors between peak potential and $\ln v$. (f) DA current response under various pH levels. (g) Fitting curve of potential vs. pH. (h) Chronocoulometry behaviors of SPE (#1), ZIF-8/SPE (#2), HZIF(Au_{4.5})/SPE (#3), HZIF(Au_{4.5})/TCPP(Fe)/SPE (#4), and HZIF(Au_{4.5})/TCPP(Fe)-Fe/SPE (#5). (i) The functional relationship between Q and $t^{1/2}$. (j) Chronoamperometric plots of HZIF(Au_{4.5})/TCPP(Fe)-Fe/SPE with various DA concentrations. (k) Linear dependence of the current signal on $t^{-1/2}$. (l) Linear relationship between slope (generated via chronoamperometric approach) and C_{DA} .

indicating a saturation of DA at the electrode interface (Figure S15b).

3.3 Quantitative analysis of DA

In order to evaluate the electroanalytical behavior of HZIF(Au_{4.5})/TCPP(Fe)-Fe/SPE subjected our material to increasing concentration of DA molecules ($C_{\text{DA}} = 0.006, 0.06, 0.6, 2, 5, 10, 50, 100, 300, 500, 700, 900, 1100, 1300, \text{ and } 1500 \mu\text{mol L}^{-1}$). This resulted in an observed direct relationship where the current signal increased with C_{DA} (Figure 6a, Figure S16). When plotting the relationship between C_{DA} and peak current (Figure 6b, Figure S17), we found that there was a linear relationship between the two groups in the region of 0.006–1500 $\mu\text{mol L}^{-1}$ with fitted linear equations, which can be seen in the Supporting Information online

(Eqs. (S9) and (S10)). The magnified linear range (0.006–10 $\mu\text{mol L}^{-1}$, marked in red) can be found in Figure S17. We then calculated the detection limit of DA on the constructed HZIF(Au_{4.5})/TCPP(Fe)-Fe electroanalytical sensing platform and determined it to be 0.002 $\mu\text{mol L}^{-1}$ ($S/N = 3$). While evaluating these data points together, we analyzed the two linear intervals (0.006–10 $\mu\text{mol L}^{-1}$, 10–1500 $\mu\text{mol L}^{-1}$) obtained in this study which can be ascribed to the fact that as the DA concentration increases, the dominant role of the electrode interface changes from the initial adsorption control to the diffusion control [47,48]. This, in turn, reduces the sensitivity of the latter interval. Meanwhile, the sensitivity of HZIF(Au_{4.5})/TCPP(Fe)-Fe electroanalytical platform to DA was calculated as 1.5774 and 5.9355 $\mu\text{A } \mu\text{M cm}^{-2}$. Specifically, the sensitivity was acquired based on the ratio of the linear slope to ERE. As illustrated in Table S4, the fabricated HZIF(Au_{4.5})/TCPP(Fe)-Fe/SPE in this work

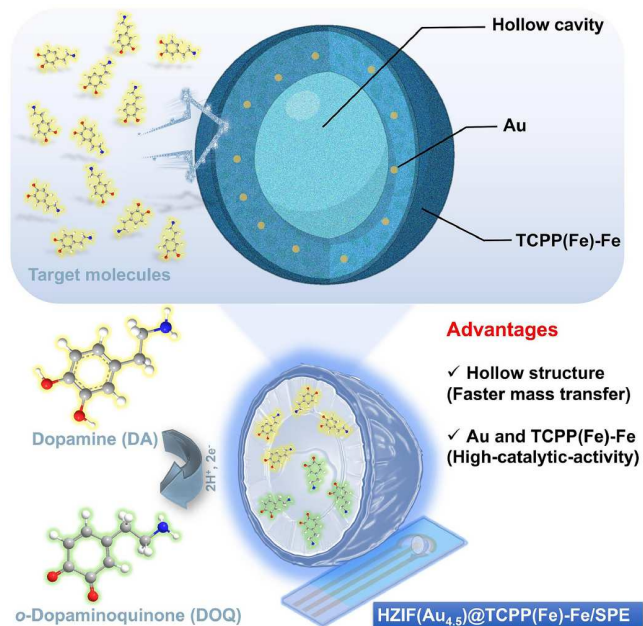


Figure 5 (Color online) Description of the electrocatalytic mechanism of DA.

displayed an improved linearity window and detection limit in comparison to similar DA electrochemical detection methods [49–61]. This excellent electroanalytical performance can be attributed to: (1) a short-range diffusion path of the hollow MOF structure, which is conducive to the transmission and contact of DA; (2) the ability of TCPP(Fe)-Fe to expose more active sites; and (3) the electron-rich Au's excellent electrochemical response to DA. Together, these advantages and the novel use of the Kirkendall effect with pure-phase nano-MOFs represent a notable advancement in the field, outcompeting other analysis techniques and offering insights that may provide new avenues for the detection of neurotransmitters.

3.4 Research on anti-interference and stability

To explore the anti-interference ability, repeatability, reproducibility, and stability of the HZIF(Au_{4.5})@TCPP(Fe)-Fe electroanalytical sensing platform, we selected a number of representative disruptors. These included, ion disruptors: NH₄⁺, Co²⁺, Cr³⁺, Fe³⁺, Zn²⁺, Ti⁴⁺, Ca²⁺, and Na⁺; analogous interferents: adrenaline, gallic acid, quercetin, 2,4,6-trichlorophenol, luteolin, catechol, estradiol, chlorogenic acid, levodopa and hydroquinone; and biomolecular disruptors: folate, hypoxanthine, glucose, thymine, hydroxylamine,

L-cysteine and sorbic acid. Each of these was tested at a concentration of 10 mmol L⁻¹, roughly 100 times that of C_{DA}. Further speaking, the observed current fluctuation of the HZIF-(Au_{4.5})@TCPP(Fe)-Fe sensor could remain relatively stable despite the interference of several times the concentration of metal ions, analogs, and biomolecule disruptors (Figure 7a–d). Further testing revealed more satisfactory characteristics of the platform. When the sensor was exposed to classical interfering substances, including ascorbic acid (*i.e.*, AA) and uric acid (*i.e.*, UA), which interfere with the detection of DA, the current response was only slightly affected, with 91.1% by the interference of AA, and UA showed no significant interference with the current signal (Figure S18). This observation was reflected in all interference studies, indicating little to no relationship between the presence of interfering agents and the detection of DA (Figure 7e). Additionally, the results of electrochemical cycling in AA and UA were shown in Figure S19. Specifically, when DPV cycling was performed in solutions containing UA and AA, the current signals of DA at this time could reach 97.1% and 89.6% of the initial values, respectively. Therefore, compared to AA, the HZIF(Au_{4.5})@TCPP(Fe)-Fe electrochemical sensor shows superior cycling stability in a solution containing UA. The HZIF(Au_{4.5})@TCPP(Fe)-Fe electrochemical sensor exhibits excellent anti-interference capabilities may be related to the following factors. The unique pore volume and pore size of HZIF-(Au_{4.5})@TCPP(Fe)-Fe nanocrystals allow the formation of channels appropriate for the transport of the target analyte (dopamine) and electron transfer. These transmission channels can depend on their shape or size to create the “size exclusion effect”, which is beneficial to improve the selectivity of the target molecules [62]. Furthermore, when seventeen individual HZIF(Au_{4.5})@TCPP(Fe)-Fe/SPE sensors were constructed using the same method for DA detection, the relative standard deviation (R.S.D) of the electroanalytical system was calculated to only vary by 4.81% (Figure 7f). Additionally, when the HZIF(Au_{4.5})@TCPP(Fe)-Fe sensor underwent the 17 consecutive DPV scans, the R.S.D. of the current only varied by 3.66% (Figure 7g). Finally, to determine the platform stability, the sensor was monitored over the course of a 35-day period, after which it retained 94% of its current response (Figure 7h). These experimental results showcase the excellent anti-interference ability and stability of the HZIF(Au_{4.5})@TCPP(Fe)-Fe portable electroanalytical sensor.

3.5 Assessment of real-world samples

To evaluate the applicability of our electroanalytical sensor toward real-world samples, we performed electrochemical analysis to detect the presence of DA in classical human serum/urine and fresh pork.

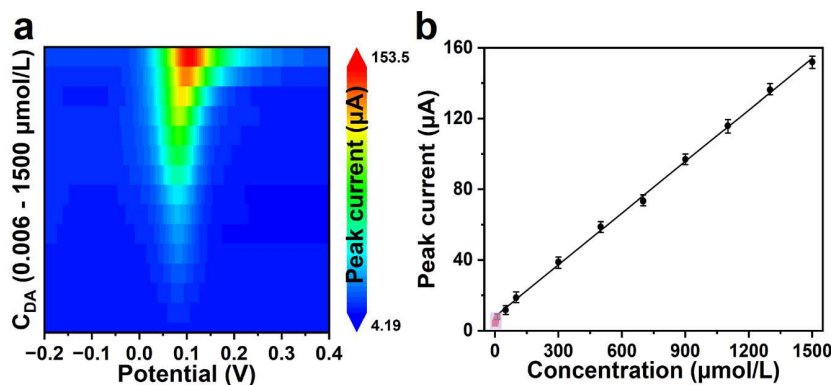


Figure 6 (Color online) (a) Contour mapping of HZIF(Au_{4.5})@TCPP(Fe)-Fe/SPE under different C_{DA} (0.006, 0.06, 0.6, 2, 5, 10, 50, 100, 300, 500, 700, 900, 1100, 1300, and 1500 μmol L⁻¹) in 0.1 mol L⁻¹ PBS (pH = 7.4). (b) Linear response of current to DA.

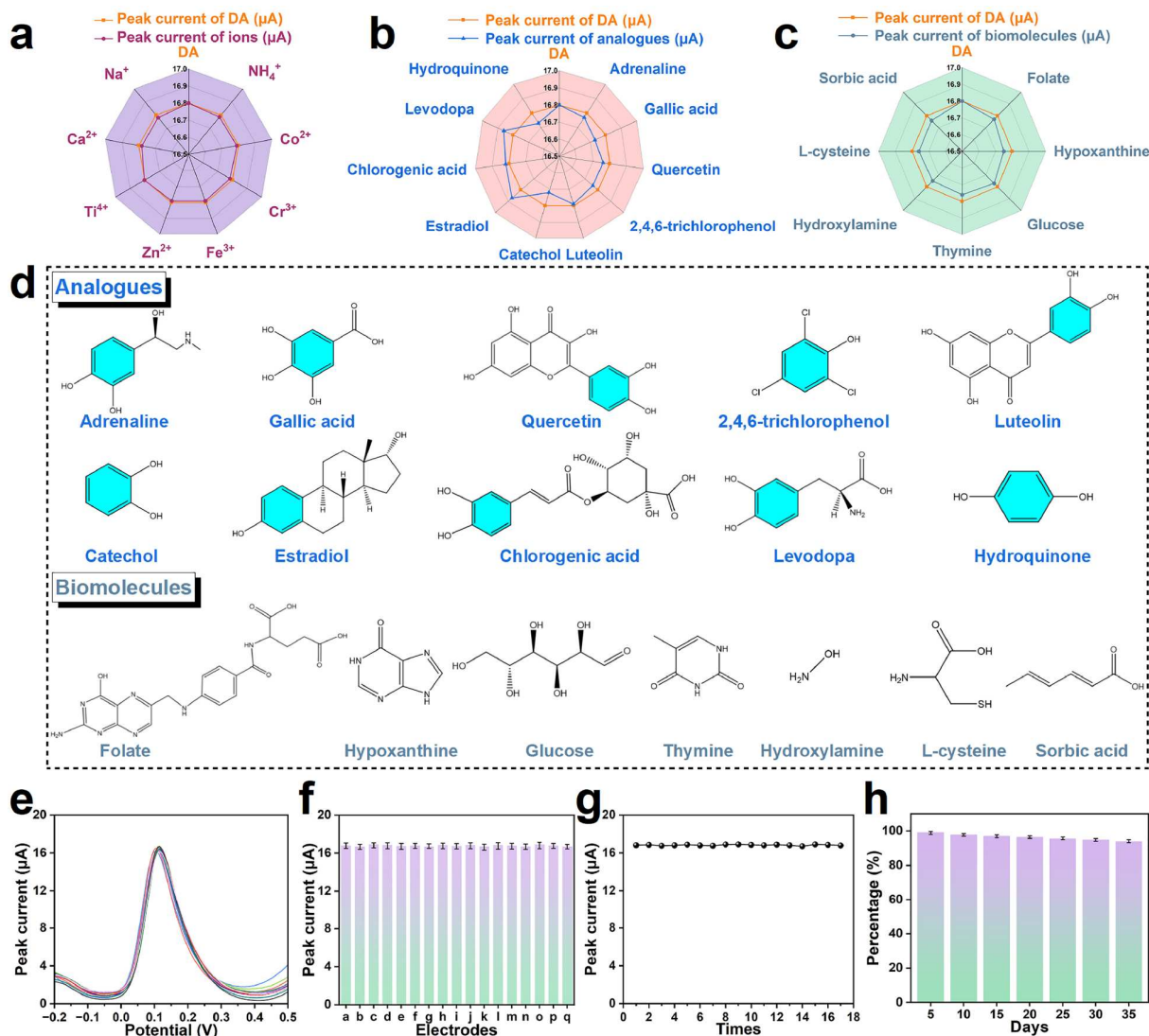


Figure 7 (Color online) Radar graphs of the effects of different kinds of interfering substances on DA current (ion interference (a), analogues interference (b), and biomolecule interference (c)). (d) Specific structure of interfering substances. (e) DPV profiles in HZIF(Au_{4.5})@TCPP(Fe)-Fe/SPE containing a range of interfering substances. (f) Current response of 17 independent HZIF(Au_{4.5})@TCPP(Fe)-Fe/SPE. 17 times consecutive DPV assessments (g) and stability exploration (h) in HZIF(Au_{4.5})@TCPP(Fe)-Fe/SPE under optimal conditions.

For the human serum/urine samples which were acquired from a local hospital in Yangzhou, we injected increasing concentrations of DA from 0.0, 15.0, 100.0, and 500.0 $\mu\text{mol L}^{-1}$ to the samples for examination. For our fresh pork samples, we obtained pig brains from the farmers' markets. During testing, we took ~ 4.7 g of sample and placed it in a 100 mL 0.1 mol L^{-1} PBS solution, which was then brought to a viscous state using a multifunctional pulverizer for 10 min. Next, zinc salt (1 M, 10 mL) was added to the mixture and before thorough mixing. After the mixture was homogenized, it was allowed to sit at 4 °C for 0.5 h. The acquired samples were then centrifuged (4000 r, 10 min) and refrigerated for subsequent evaluation. Each of these samples, from both groups, was further processed via filtration to improve the accuracy of the results prior to testing. During electroanalytical evaluation, we observed that the overall recovery rates of tests ranged from 97.9% to 102.0% with the relative standard deviation (R.S.D.) varying by only $\leq 3.4\%$ (Table S5). In addition, this electroanalytical sensing platform also reached 84.5% and 86.6% current values after electrochemical cycling in real serum and urine samples, respectively (Figures S20 and S21). When compared using high-performance liquid chromatography (HPLC), which represents traditional methods, we found that these results were consistent with our electroanalytical

method. To further support our results, we compared the groups using the classical statistical tools (F-test and t-test), which demonstrate that there is no significant difference in the assessment results between the two techniques. These results illustrate the exceptional potential of the constructed electrochemical sensing platform in real-world conditions, which may be leveraged directly in applications or expanded upon toward the detection of other critical solutes.

4 Conclusions

This work presents a novel approach to detect DA and possibly other critical solutes via an HZIF(Au_{4.5})@TCPP(Fe)-Fe electrocatalyst for electrochemical detection. By leveraging the Kirkendall effect of solid ZIF-8, an obvious hollow structure could be acquired after 1 h, which promotes rapid transport of DA. This is made possible by the unique metallization cross-linking engineering (TCPP(Fe)-Fe), which significantly enhances the electroanalytical signal of DA in conjunction with the regulation of electronic states, enabling the presence of abundant electron-rich Au species within the system, which provides excellent electrochemical performance. Together, these attributes allowed the electroanalytical sensing platform to

detect in a satisfactory linear window (0.006–1500 $\mu\text{mol L}^{-1}$) with a limit of detection (0.002 $\mu\text{mol L}^{-1}$, S/N = 3). The HZIF(Au_{4.5})@TCPP(Fe)-Fe electrochemical sensor also achieved a good signal response while in the presence of a series of interfering metal ions, analogues and biomolecules. These results demonstrate the outstanding repeatability, reproducibility, storage stability, and the feasibility of this device for samples and applications. Together, the integration of strategies based on the Kirkendall effect, metalloporphyrins, and cross-linking engineering allows us to offer a novel method for electroanalytical detection using porous coordination nanocomposites with exceptional detection and stability characteristics.

Conflict of interest

The authors declare no conflict of interest.

Acknowledgement

This work was supported by the National Natural Science Foundation of China (22174124), the Fundamental Research Funds for the Central Universities (KLSB2024KF-04) and the Postgraduate Research & Practice Innovation Program of Jiangsu Province (Yangzhou University) (KYCX24_3717). Partial support from the Robert A. Welch Foundation (B-0027) (Shengqian Ma) and Princess Nourah bint Abdulrahman University Researchers Supporting Project (PNURSP2025R1), Riyadh, Saudi Arabia (Thamraa AlShahrani) is also acknowledged.

Supporting information

The supporting information is available online at chem.scichina.com and link.springer.com/journal/11426. The supporting materials are published as submitted, without typesetting or editing. The responsibility for scientific accuracy and content remains entirely with the authors.

References

- Tian H, Liang J, Liu J. *Adv Mater*, 2019, 31: 1903886
- Zhao M, Wang X, Yang X, Gilroy KD, Qin D, Xia Y. *Adv Mater*, 2018, 30: 1801956
- Lu Y, Zhang G, Zhou H, Cao S, Zhang Y, Wang S, Pang H. *Angew Chem Int Ed*, 2023, 62: e202311075
- Liu L, Chen XL, Cai M, Yan RK, Cui HL, Yang H, Wang JJ. *Chin Chem Lett*, 2023, 34: 108411
- Wang CY, Liu YQ, Jia C, Zhang MZ, Song CL, Xu C, Hao R, Qin JC, Yang YW. *Chin Chem Lett*, 2023, 34: 108400
- Xu Z, Chen H, Chu H, Shen X, Deng C, Sun N, Wu H. *Chin Chem Lett*, 2023, 34: 107829
- Xia Y, Su T, Mi Z, Feng Z, Hong Y, Hu X, Shu Y. *Anal Chim Acta*, 2023, 1278: 341754
- Wei Y, Zheng M, Zhu W, Zhang Y, Hu W, Pang H. *J Colloid Interface Sci*, 2023, 631: 8–16
- Shu Y, Yan L, Ye M, Chen L, Xu Q, Hu X. *Analyst*, 2023, 148: 4721–4729
- Wang F, Hu J, Wu X, Yuan G, Su Y, Fan Z, Xue H, Pang H. *J Colloid Interface Sci*, 2024, 665: 764–771
- Cao S, Lu Y, Tang Y, Sun Y, Zhou H, Zhang G, Lin X, Pang H. *J Colloid Interface Sci*, 2024, 654: 466–475
- Xia Y, Shi F, Liu R, Zhu H, Liu K, Ren C, Li J, Yang Z. *Anal Chem*, 2024, 96: 1345–1353
- Wang H, Zheng F, Xue G, Wang Y, Li G, Tang Z. *Sci China Chem*, 2021, 64: 1854–1874
- Qiu T, Gao S, Liang Z, Wang D, Tabassum H, Zhong R, Zou R. *Angew Chem Int Ed*, 2021, 60: 17314–17336
- Zhu R, Xie L, Zhang Y, Liu L, Jiang Y, Pang H. *Inorg Chem*, 2024, 63: 13093–13099
- Sun L, Lv H, Feng J, Guselnikova O, Wang Y, Yamauchi Y, Liu B. *Adv Mater*, 2022, 34: 2201954
- Wang X, Feng J, Bai Y, Zhang Q, Yin Y. *Chem Rev*, 2016, 116: 10983–11060
- Zhu L, Zhu Z, Zhou J, Qian Y. *Chem Commun*, 2020, 56: 11795–11798
- Liu X, Liu Y, Zhang C, Chen Y, Luo G, Wang Z, Wang D, Gao S. *Chem Eng J*, 2023, 473: 145135
- Singh R, Mukherjee A. *ACS Catal*, 2019, 9: 3604–3617
- Yao S, Zhao X, Wan X, Wang X, Huang T, Zhang J, Li L. *Mater Horiz*, 2021, 8:

- 3457–3467
- Li Y, Gao Z, Chen F, You C, Wu H, Sun K, An P, Cheng K, Sun C, Zhu X, Sun B. *ACS Appl Mater Interfaces*, 2018, 10: 30930–30935
- Hassanzadeh Goji N, Ramezani M, Sh. Saljooghi A, Alibolandi M. *J Nanostruct Chem*, 2024, 14: 167–208
- Xi X, Tang W, Wu D, Shen C, Ji W, Li J, Su Y, Guo X, Liu R, Yan F. *ACS Sens*, 2023, 8: 1211–1219
- Yan T, Zhang XY, Zhao Y, Sun WY. *J Mater Chem A*, 2023, 11: 268–275
- Li J, Shen H, Yu S, Zhang G, Ren C, Hu X, Yang Z. *Analyst*, 2020, 145: 3283–3288
- Jiang J, Wang J, Wang P, Lin X, Diao G. *J Electroanal Chem*, 2023, 928: 117056
- Zhu R, Song Y, Hu J, Zhu K, Liu L, Jiang Y, Xie L, Pang H. *Chem Eur J*, 2024, 30: e202400982
- Yang C, Wang Q, Zhang KL. *Dalton Trans*, 2023, 52: 5687–5703
- Sun W, Liu J, Chu H, Wang Y. *Microchim Acta*, 2024, 191: 48
- Zhang D, Liu J, Du P, Zhang Z, Ning X, Deng Y, Yin D, Chen J, Han Z, Lu X. *Small*, 2020, 16: 1905889
- Tang L, Zhang S, Wu Q, Wang X, Wu H, Jiang Z. *J Mater Chem A*, 2018, 6: 2964–2973
- Li X, Yang G, Li S, Xiao N, Li N, Gao Y, Lv D, Ge L. *Chem Eng J*, 2020, 379: 122350
- Zhu Z, Ni Y, Lv Q, Geng J, Xie W, Li F, Chen J. *Proc Natl Acad Sci USA*, 2021, 118: e2024619118
- Mortada B, Chaplais G, Veremeienko V, Nouali H, Marichal C, Patarin J. *J Phys Chem C*, 2018, 122: 3846–3855
- Lv Z, Meng X, Liang Q, Jiang T, Sun S, Tan Y, Feng J. *Int J Biol Macromol*, 2024, 259: 129249
- Zhang Y, Tong Y, Li X, Guo S, Zhang H, Chen X, Cai K, Cheng L, He W. *ACS Omega*, 2021, 6: 18566–18575
- Chaplais G, Fraux G, Paillaud JL, Marichal C, Nouali H, Fuchs AH, Coudert FX, Patarin J. *J Phys Chem C*, 2018, 122: 26945–26955
- Cui Z, Li T, Sun J, Li Q, Zhang H, Li GY. *Sep Purif Tech*, 2024, 351: 128152
- Rayati S, Nafarieh P. *Appl Org Chem*, 2019, 33: e4789
- Wang H, Liu X, Yang W, Mao G, Meng Z, Wu Z, Jiang HL. *J Am Chem Soc*, 2022, 144: 22008–22017
- Wang H, Liu X, Zhao Y, Sun Z, Lin Y, Yao T, Jiang HL. *Natl Sci Rev*, 2024, 11: nwae252
- Mukhopadhyay RD, Kim Y, Koo J, Kim K. *Acc Chem Res*, 2018, 51: 2730–2738
- Ning X, Lu B, Zhang Z, Du P, Ren H, Shan D, Chen J, Gao Y, Lu X. *Angew Chem Int Ed*, 2019, 58: 16800–16805
- Wang Z, Jin H, Meng T, Liao K, Meng W, Yang J, He D, Xiong Y, Mu S. *Adv Funct Mater*, 2018, 28: 1802596
- Mutić S, Đurđić S, Petrović S, Gemeiner P, Stanković D, Anojić J. *Electrochim Acta*, 2024, 500: 144755
- Yue HY, Huang S, Chang J, Heo C, Yao F, Adhikari S, Gunes F, Liu LC, Lee TH, Oh ES, Li B, Zhang JJ, Huy TQ, Luan NV, Lee YH. *ACS Nano*, 2014, 8: 1639–1646
- Zhang T, Chen Y, Huang W, Wang Y, Hu X. *Sens Actuat B-Chem*, 2018, 276: 362–369
- Huang H, Yue Y, Chen Z, Chen Y, Wu S, Liao J, Liu S, Wen H. *Microchim Acta*, 2019, 186: 189
- Qi S, Zhao B, Tang H, Jiang X. *Electrochim Acta*, 2015, 161: 395–402
- Wang C, Du J, Wang H, Zou C, Jiang F, Yang P, Du Y. *Sens Actuat B-Chem*, 2014, 204: 302–309
- Emran MY, Shenashen MA, Morita H, El-Safty SA. *Biosens Bioelectron*, 2018, 109: 237–245
- Aparna TK, Sivasubramanian R, Dar MA. *J Alloys Compd*, 2018, 741: 1130–1141
- Du J, Yue R, Ren F, Yao Z, Jiang F, Yang P, Du Y. *Biosens Bioelectron*, 2014, 53: 220–224
- Zheng X, Zhou X, Ji X, Lin R, Lin W. *Sens Actuat B-Chem*, 2013, 178: 359–365
- Zhang X, Zhang YC, Ma LX. *Sens Actuat B-Chem*, 2016, 227: 488–496
- Immanuel S, Aparna TK, Sivasubramanian R. *Surfs Interfaces*, 2019, 14: 82–91
- Ma L, Zhang Q, Wu C, Zhang Y, Zeng L. *Anal Chim Acta*, 2019, 1055: 17–25
- Lei P, Zhao S, Asif M, Aziz A, Zhou Y, Dong C, Li M, Shuang S. *Langmuir*, 2024, 40: 11635–11641
- Tashkhourian J, Sheydaei O, Nami-Ana SF. *Appl Org Chem*, 2018, 32: e4196
- Thirumalraj B, Rajkumar C, Chen SM, Palanisamy S. *Sci Rep*, 2017, 7: 41213
- Wang K, Li C, Liang Y, Han T, Huang H, Yang Q, Liu D, Zhong C. *Chem Eng J*, 2016, 289: 486–493